Efficient Mixed-Domain Analysis of Electrostatic MEMS

Gang Li, *Student Member, IEEE,* and N. R. Aluru, *Member, IEEE*

Abstract—We present efficient computational methods for scattered point and meshless analysis of electrostatic microelectromechanical systems (MEMS). Electrostatic MEM devices are governed by coupled mechanical and electrostatic energy domains. A self-consistent analysis of electrostatic MEMS is implemented by combining a finite cloud method-based interior mechanical analysis with a boundary cloud method (BCM)-based exterior electrostatic analysis. Lagrangian descriptions are used for both mechanical and electrostatic analyses. Meshless finite cloud and BCMs, combined with fast algorithms and Lagrangian descriptions, are flexible, efficient, and attractive alternatives compared to conventional finite element/boundary element methods for self-consistent electromechanical analysis. Numerical results are presented for MEM switches, a micromirror device, a lateral comb drive microactuator, and an electrostatic comb drive device. Simulation results are compared with experimental and previously reported data for many of the examples discussed in this paper and a good agreement is observed.

Index Terms—Boundary cloud method (BCM), coupled electromechanical analysis, finite cloud method (FCM), lagrangian electrostatics, meshless methods.

I. INTRODUCTION

ADVANCES in micromachining technology have enabled the design and development of micromechanical sensors, actuators, devices, and systems [1]. A few examples include micromachined accelerometers for automatic airbag deployment, micromachined mirror arrays for high-performance projection displays, pressure sensors, microfluidic technology-based lab-on-a-chip, chemical, and biological sensors and other devices. Many of these devices were designed and fabricated using a physical prototyping approach involving several design cycles. The physical prototyping approach based on expensive and multiyear design and fabrication cycles can be significantly shortened by fast and accurate computational prototyping tools [2]. Computational prototyping tools based on hierarchical or structured design methodologies have started to emerge recently [3]–[8]. In a structured design methodology, simulation tools are developed for four primary steps, namely, process simulation tools, device simulation tools, circuit simulation

G. Li is with the Department of Mechanical and Industrial Engineering, Beckman Institute for Advanced Science and Technology, University of Illinois, Urbana–Champaign, IL 61801 USA.

N. R. Aluru is with the Department of General Engineering, Beckman Institute for Advanced Science and Technology, University of Illinois, Urbana–Champaign, IL 61801 USA (e-mail: aluru@uiuc.edu).

tools, and system-level simulation tools. The focus of this paper is on the development of efficient computational prototyping tools for device-level modeling of MEMS.

Although there are many microelectromechanical system designs that use piezoelectric, thermal, pneumatic, and magnetic actuation (see, e.g., [9], for an overview), the most popular approach in present day microsensor and microactuator designs is to use electrostatic forces to move micromachined parts. Electrostatically actuated microstructures are also referred to as electrostatic MEMS. Computational analysis of electrostatic MEMS requires a self-consistent solution of the coupled interior mechanical domain and the exterior electrostatic domain [2], [10], [11]. Conventional methods for coupled-domain analysis, such as finite element method (FEM)/boundary element method (BEM), require mesh generation, mesh compatibility, remeshing, and interpolation of solution between the domains. Mesh generation can be difficult and time consuming for complex geometries. Furthermore, mesh distortion can occur for micromechanical structures that undergo large deformations. To overcome all of these difficulties, we propose an efficient approach to perform static analysis of electrostatically actuated MEMS. The primary contributions of the paper are as follows:

1) We employ a meshless finite cloud method (FCM) [12], [13] to solve the interior mechanical domain. The FCM is a true meshless method in which only points are needed to cover the structural domain and no connectivity information among the points is required. This method completely eliminates the meshing process and radically simplifies the analysis procedure.

2) A boundary cloud method (BCM) [14], [15] is used to analyze the exterior electrostatic domain to compute the electrostatic forces acting on the surface of the conductors. BCM utilizes a meshless interpolation technique and a cell based integration. Besides the flexibility of the cell integration, BCM is an excellent match to FCM for coupled-domain analysis as both of them have meshless interpolations.

3) A Lagrangian description [16] of the boundary integral equation is developed and implemented with BCM. Typically, the mechanical analysis is performed by a Lagrangian approach using the undeformed position of the structures. However, the electrostatic analysis is performed by using the deformed position of the conductors. The Lagrangian description maps the electrostatic analysis to the undeformed position of the conductors. Thus, the electrostatic forces and mechanical deformations are all computed on the undeformed configuration of the structures. The Lagrangian description eliminates
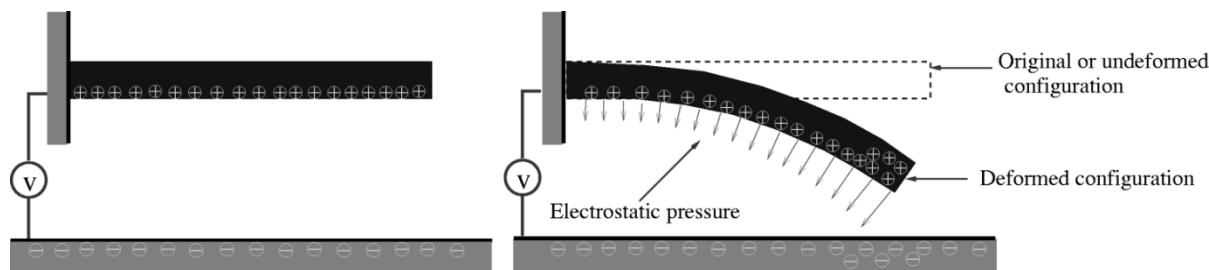
Fig. 1. Illustration of coupling in electrostatic MEMS through a simple example. A cantilever beam over a ground plane (a) applied voltage causes a charge distribution and (b) the deformed structure with charge redistribution.

the requirement of geometry updates and recomputation of the interpolation functions.

The rest of the paper is organized as follows. Section II describes the techniques for coupled analysis of electromechanical systems, Section III introduces the FCM for mechanical analysis, Section IV describes the Lagrangian formulation for electrostatics, Section V introduces the BCM for electrostatic analysis, numerical results are shown in Section VI, and a conclusion is given in Section VII.

II. COUPLED ANALYSIS OF ELECTROMECHANICAL SYSTEMS

Computational analysis of electrostatically actuated MEMS requires a self-consistent solution of the coupled mechanical and electrical equations. To understand the current approach for self-consistent analysis of electrostatic MEMS, consider the simple example, a cantilever beam over a ground plane, as shown in Fig. 1. When a voltage is applied between the cantilever beam and the ground plane, electrostatic charges are induced on the surface of the conductors. These charges give rise to electrostatic pressure, which acts normal to the surface of the conductors. Since the ground plane is fixed and cannot move, the electrostatic pressure deforms only the cantilever beam. When the beam deforms, the charge redistributes on the surface of the conductors and, consequently, the resultant electrostatic pressure and the deformation of the beam also change. This process continues until an equilibrium state is reached.

Conventionally, an FEM [17] is employed to perform the mechanical analysis, and a BEM [18] is employed to compute the surface charge densities. The mechanical analysis is performed by discretizing the structural or the mechanical domain into nodes and elements. A finite element analysis is then performed by applying the electrostatic pressure as Neumann boundary conditions to compute the structural displacements. Once the displacement is computed, the geometry of the structure or the conductor is updated. Electrostatic analysis is performed on the updated geometry by discretizing the surface of the conductor into panels or elements. A BEM is then used to compute the surface charge density on each panel. Once the surface charge densities are known, the new electrostatic pressure is computed. The mechanical and electrostatic analysis are repeated until an equilibrium state is computed. Algorithm 1 summarizes the key steps involved in the self-consistent solution of the coupled electromechanical problem.

```
Algorithm 1 A procedure for
self-consistent analysis of coupled
electromechanical devices
repeat
 1. Do mechanical analysis (on the unde-
 formed geometry) to compute structural
 displacements
 2. Update the geometry of the conductors
 using the computed displacements
 3. Compute surface charge density by
 electrostatic analysis (on the deformed
 geometry)
 4. Compute electrostatic pressure (on the
 deformed geometry)
 5. Transform electrostatic pressure to
 the original undeformed configuration
until an equilibrium state is reached
```

There are several difficulties with the approach described in Algorithm 1

1) The structural domain needs to be discretized into elements. For structures with complex geometries this could be a complicated and time-consuming task.
2) Typically, the boundary element mesh on the surface of the conductors does not match with the finite element mesh. In this case, the electrostatic pressure computed from the BEM analysis needs to be interpolated to the finite element mesh so that a mechanical analysis can be performed. The interpolation process can be cumbersome and can introduce significant error. One solution to this problem is to match the finite element nodes on the surface of the conductors with the boundary element nodes so that no interpolation is involved. However, this can be inefficient as a refinement of either the finite element mesh or the boundary element mesh would require that the other domain be remeshed.
3) The need to update the geometry of the conductors before an electrostatic analysis is performed during each iteration also presents several problems. First, flat surfaces of the conductors in the initial configuration can become curved due to conductor deformation. This requires the development of complex integration schemes on curved panels [20] to perform electrostatic analysis. Second, when the structure undergoes very large deformation, remeshing the surface may become necessary before an electrostatic analysis is performed. Third, interpo-

lation functions, used in many numerical methods, need to be recomputed whenever the geometry changes. Each of these issues significantly increases the computational effort making the self-consistent analysis of electrostatic MEMS an extremely complex and challenging task.

The combination of the FCM, BCM, and the Lagrangian electrostatics approach overcomes the difficulties mentioned above. First, an FCM does not require a mesh or elements and mechanical analysis can be performed by simply sprinkling points without the need for connectivity information among the nodes or points. Second, using a BCM, exterior electrostatic analysis is performed by sprinkling points on the surface of the conductors and using a background cell structure for integration purpose. Unlike a BEM, the BCM does not require panels or elements. Third, by combining the Lagrangian electrostatics formulation with the total Lagrangian mechanical formulation, coupled electromechanical analysis can be implemented using only the initial configuration. The use of Lagrangian techniques for both mechanical and electrostatic analysis eliminates the need for geometry updates thereby simplifying the coupled electromechanical analysis. Algorithm 2 summarizes the full Lagrangian approach for efficient scattered point and self-consistent analysis of coupled electromechanical devices. Compared with the FEM/BEM approach, the FCM/BCM approach reduces the computational cost for the coupled electromechanical analysis by eliminating the meshing, remeshing, updating geometry, and load transformation processes. Detailed computational cost comparisons between FCM and FEM, BCM and BEM can be found in [21] and [22].

Algorithm 2 A procedure for self-consistent analysis of coupled electromechanical devices by using a full Lagrangian approach for both mechanical and electrostatic analysis
repeat
 1. Do mechanical analysis (on the undeformed geometry) by FCM to compute structural displacements
 2. Do electrostatic analysis (on the undeformed geometry) by BCM to compute surface charge density
 3. Compute electrostatic pressure (on the undeformed geometry)
until an equilibrium state is reached

III. FCM FOR MECHANICAL ANALYSIS

Electrostatically actuated microstructures can undergo large deformations for certain geometric configurations and applied voltages. In this paper, we perform two-dimensional (2-D) geometrically nonlinear analysis of microstructures. For electromechanical analysis, the governing equations for an elastic body using a Lagrangian description are given by [23]

$$\nabla \cdot (\mathbf{F}\mathbf{S}) + \mathbf{B} = 0 \text{ in } \Omega \tag{1}$$

$$\mathbf{u} = \mathbf{G} \text{ on } \Gamma_g \tag{2}$$

$$\mathbf{P} \cdot \mathbf{N} = \mathbf{H} \text{ on } \Gamma_h \tag{3}$$

where Ω is the mechanical domain, Γ_g is the portion of the boundary on which Dirichlet boundary conditions are specified, and Γ_h is the portion of the boundary on which Neumann boundary conditions are specified. The boundary of the mechanical domain is given by $\Gamma = \Gamma_g \cup \Gamma_h$. $\mathbf{F}$ is the deformation gradient given by

$$\mathbf{F} = \mathbf{I} + \nabla \mathbf{u} \tag{4}$$

where $\mathbf{u}$ is the displacement vector from the initial configuration $\mathbf{X}$ to the deformed configuration $\mathbf{x}$, $\mathbf{x} = \mathbf{X} + \mathbf{u}$, $\mathbf{I}$ is identity tensor, $\mathbf{N}$ is the unit outward normal vector in the initial configuration and $\mathbf{S}$ is the second Piola–Kirchhoff stress given by

$$\mathbf{S} = \mathbf{C}\mathbf{E} \tag{5}$$

where $\mathbf{C}$ is the material tensor and $\mathbf{E}$ is the Green–Lagrangian strain

$$\mathbf{E} = \frac{1}{2}(\mathbf{F}^T\mathbf{F} - \mathbf{I}). \tag{6}$$

$\mathbf{B}$ is the body force vector per unit undeformed volume, $\mathbf{G}$ is the prescribed displacement vector and $\mathbf{P}$ is the first Piola–Kirchhoff stress tensor given by

$$\mathbf{P} = \mathbf{F}\mathbf{S}. \tag{7}$$

$\mathbf{H}$ is the surface traction vector per unit undeformed area. For electromechanical analysis, $\mathbf{H}$ is given by

$$\mathbf{H} = P_e J \mathbf{F}^{-T} \mathbf{N} \tag{8}$$

where P_e is the surface electrostatic pressure and J is the determinant of $\mathbf{F}$.

We use a meshless FCM (e.g., see [24] for an overview on meshless methods) to solve the mechanical equations given in (1)–(3). The meshless FCM uses a fixed-kernel technique to construct the interpolation functions and a point collocation technique to discretize the governing partial differential equations. In a 2-D fixed kernel approach, an approximation $u^a(x,y)$ to an unknown $u(x,y)$ is given by

$$u^a(x,y) = \int_\Omega \mathcal{C}(x,y,x_k-s,y_k-t)\phi(x_k-s,y_k-t)u(s,t)dsdt \tag{9}$$

where ϕ is the kernel function centered at (x_k, y_k) which is usually taken as a cubic spline or a Gaussian function. In this paper, ϕ is taken as a modified Gaussian function, i.e.,

$$\phi(x - x_I) = \frac{w(x - x_I)}{1 - w(x - x_I) + \hat{\epsilon}} \tag{10}$$

where $\hat{\epsilon}$ is a small number which is used to avoid the singularity of $\phi(x - x_I)$. In this paper, $\hat{\epsilon}$ is chosen to be 10^{-5}. $w(x - x_I)$ is a normalized Gaussian function given by

$$w(z) = \begin{cases} \frac{e^{-(z/c)^2} - e^{-(d_{\text{mi}}/c)^2}}{1 - e^{-(d_{\text{mi}}/c)^2}} & z \leq d_{mi} \\ 0 & z > d_{\text{mi}} \end{cases} \tag{11}$$

where d_{mi} is the support size of a cloud, c is the dilation parameter which is taken as $d_{\mathrm{mi}}/2$. In two dimensions, the kernel function is constructed as

$$\phi(x - x_I, y - y_I) = \phi(x - x_I)\phi(y - y_I). \qquad (12)$$

$\mathcal{C}(x, y, x_k - s, y_k - t)$ is the correction function which is given by

$$\mathcal{C}(x, y, x_k - s, y_k - t) = \mathbf{p}^T(x_k - s, y_k - t)\mathbf{c}(x, y) \qquad (13)$$

$\mathbf{p}^T = \{p_1, p_2, \ldots, p_m\}$ is an $m \times 1$ vector of basis functions. In two dimensions, a quadratic basis vector is given by

$$\mathbf{p}^T = \left[1, x_k - s, y_k - t, (x_k - s)^2, (x_k - s)(y_k - t), (y_k - t)^2\right]$$
$$m = 6 \qquad (14)$$

$\mathbf{c}(x, y)$ is an $m \times 1$ vector of unknown correction function coefficients. The correction function coefficients are computed by satisfying the consistency conditions, i.e.,

$$\int_\Omega \mathbf{p}^T(x_k - s, y_k - t)\mathbf{c}(x, y)\phi(x_k - s, y_k - t)$$
$$\cdot p_i(s, t)\,ds\,dt = p_i(x, y) \qquad i = 1, 2, \ldots, m. \qquad (15)$$

In discrete form, (15) can be written as

$$\sum_{I=1}^{NP} \mathbf{p}^T(x_k - x_I, y_k - y_I)\mathbf{c}(x, y)\phi(x_k - x_I, y_k - y_I)$$
$$\cdot p_i(x_I, y_I)\Delta V_I = p_i(x, y) \qquad i = 1, 2, \ldots, m. \qquad (16)$$

where NP is the number of points in the domain and ΔV_I is the nodal volume of node I (see [12] for a discussion on nodal volumes). Equation (16) can be written in a matrix form as

$$\mathbf{M}\mathbf{c}(x, y) = \mathbf{p}(x, y) \qquad (17)$$
$$M_{ij} = \sum_{I=1}^{NP} p_j(x_k - x_I, y_k - y_I)\phi(x_k - x_I, y_k - y_I)$$
$$\cdot p_i(x_I, y_I)\Delta V_I$$
$$i, j = 1, 2, \ldots, m. \qquad (18)$$

From (17), the unknown correction function coefficients are computed as

$$\mathbf{c}(x, y) = \mathbf{M}^{-1}\mathbf{p}(x, y). \qquad (19)$$

Substituting the correction function coefficients into (13) and employing a discrete approximation for (9), we obtain

$$u^a(x, y) = \sum_{I=1}^{NP} N_I(x, y)\hat{u}_I \qquad (20)$$

where $\hat{u}_I$ is the nodal parameter for node I and $N_I(x, y)$ is the fixed kernel meshless interpolation function defined as

$$N_I(x, y) = \mathbf{p}^T(x, y)\mathbf{M}^{-T}\mathbf{p}(x_k - x_I, y_k - y_I)$$
$$\cdot \phi(x_k - x_I, y_k - y_I)\Delta V_I. \qquad (21)$$

The interpolation functions obtained by (21) are multivalued. A unique set of interpolation functions can be constructed by computing $N_I(x_k, y_k)$, $I = 1, 2, \ldots, NP$, when the kernel is centered at (x_k, y_k) (see [12] for more details). The derivatives of the unknown u are approximated by

$$\frac{\partial u^a(x, y)}{\partial x} = \sum_{I=1}^{NP} \frac{\partial N_I(x, y)}{\partial x}\hat{u}_I \qquad (22)$$

$$\frac{\partial u^a(x, y)}{\partial y} = \sum_{I=1}^{NP} \frac{\partial N_I(x, y)}{\partial y}\hat{u}_I \qquad (23)$$

$$\frac{\partial^2 u^a(x, y)}{\partial x^2} = \sum_{I=1}^{NP} \frac{\partial^2 N_I(x, y)}{\partial x^2}\hat{u}_I \qquad (24)$$

$$\frac{\partial^2 u^a(x, y)}{\partial y^2} = \sum_{I=1}^{NP} \frac{\partial^2 N_I(x, y)}{\partial y^2}\hat{u}_I \qquad (25)$$

$$\frac{\partial^2 u^a(x, y)}{\partial x \partial y} = \sum_{I=1}^{NP} \frac{\partial^2 N_I(x, y)}{\partial x \partial y}\hat{u}_I. \qquad (26)$$

In the 2-D mechanical analysis, the displacements u and v and their derivatives are approximated by using (20)–(26). Consequently, the deformation gradient $\mathbf{F}$ is approximated by

$$\mathbf{F}^a = \mathbf{I} + \nabla\mathbf{u}^a = \begin{bmatrix} 1 + \frac{\partial u^a}{\partial X} & \frac{\partial u^a}{\partial Y} \\ \frac{\partial v^a}{\partial X} & 1 + \frac{\partial v^a}{\partial Y} \end{bmatrix}. \qquad (27)$$

Thus, all of the other quantities in (5)–(7) can be rewritten as functions of the approximated displacements u^a and v^a.

After the interpolation functions are constructed, FCM uses a point collocation technique [19] to discretize the governing equations. In a point collocation approach, the governing equations are satisfied at every node which does not carry a boundary condition and, for nodes with boundary conditions, the approximate solution or the derivative of the approximate solution are set to the given Dirichlet and Neumann boundary conditions, respectively. Substituting the approximations into (1), one obtains a nonlinear system of equations of the form

$$\mathbf{f}_j(\hat{u}_1, \hat{u}_2, \ldots, \hat{u}_{NP}; \hat{v}_1, \hat{v}_2, \ldots, \hat{v}_{NP}) = 0 \qquad j = 1, 2 \quad (28)$$

where $\mathbf{f}_1$ and $\mathbf{f}_2$ refer to the equilibrium equations in the x- and y-directions, respectively. The resultant nonlinear system of equations are solved by employing a Newton's method. For nodes with Dirichlet and Neumann boundary conditions, the governing equations are set to be

$$\mathbf{u}^a - \mathbf{G} = 0 \text{ on } \Gamma_g \qquad (29)$$
$$\mathbf{P}(\mathbf{u}^a) \cdot \mathbf{N} - \mathbf{H} = 0 \text{ on } \Gamma_h \qquad (30)$$

IV. LAGRANGIAN ELECTROSTATICS

When electrostatic potentials are applied on microstructures, electrostatic forces are generated on the surfaces of the microstructures. The structures undergo deformation because of electrostatic forces and the surface charge on the structure redistributes. Typically, the new surface charge density is computed by updating the geometry of the microstructure and redoing an electrostatic analysis. The basic idea in Lagrangian
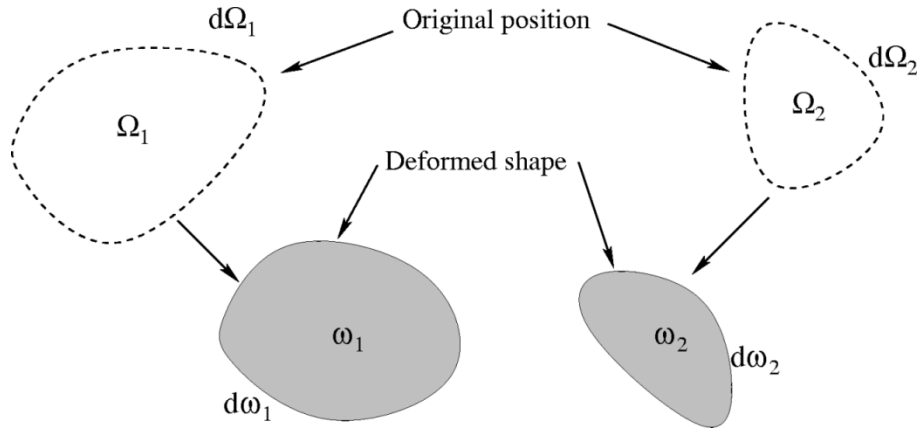
Fig. 2.   Two-conductor electrostatic system.

electrostatics is to compute the new surface charge density without updating the geometry of the microstructures.

To understand the Lagrangian electrostatics concepts, consider a two conductor system as shown in Fig. 2. Ω_1 and Ω_2 denote the original geometry of conductors 1 and 2, respectively, $d\Omega_1$ and $d\Omega_2$ denote the surface or boundary of conductors 1 and 2, respectively, ω_1 denotes the deformed shape of conductor 1, ω_2 denotes the deformed shape of conductor 2, $d\omega_1$ and $d\omega_2$ denote the deformed surfaces of conductors 1 and 2, respectively, and $\bar{\omega}$ is the domain exterior to ω_1 and ω_2. A potential of g_1 is applied on conductor 1 and a potential of g_2 is applied on conductor 2. The applied potentials do not change as the conductors undergo deformation or shape changes.

The 2-D governing equation for electrostatic analysis is given by [25]

$$\nabla^2 \phi = 0 \text{ in } \bar{\omega} \tag{31}$$
$$\phi = g_1 \text{ on } d\omega_1 \tag{32}$$
$$\phi = g_2 \text{ on } d\omega_2 \tag{33}$$

where $\bar{\omega}$ is the domain exterior to ω_1 and ω_2. An efficient approach to treat exterior electrostatic problems is to use a boundary integral equation approach where the governing partial differential equation can be rewritten in a boundary integral form as [26]

$$\phi(p) = \int_{d\omega} G(p, q)\sigma(q)d\gamma_q + C \tag{34}$$

$$\int_{d\omega} \sigma(q)d\gamma_q = C_T \tag{35}$$

where p is the source point, q is the field point which moves along the boundary of the conductors, and G is the Green's function. In two dimensions, $G(p, q) = -ln|\mathbf{x}_p - \mathbf{x}_q|/(2\pi\epsilon)$, where ϵ is the dielectric constant of the medium and $|\mathbf{x}_p - \mathbf{x}_q|$ is the distance between the source point p and the field point q. C_T is the total charge of the system and C is an unknown variable which can be used to compute the potential at infinity.

Equations (34) and (35) are defined in the deformed configuration of the conductors, i.e., the surface charge density is computed by solving the boundary integral equations on the deformed geometry of the conductors. We refer to this approach as the deformed configuration approach. The need to update the geometry of the structures in the deformed configuration approach presents several difficulties as stated in Section II. In this paper, we employ a Lagrangian approach [16] to compute the surface charge density in the undeformed configuration of the conductors.

When a material body is subjected to a force, either internal or external, its geometrical shape undergoes a change. As shown in Fig. 3, the initial configuration of a body is denoted by B (all quantities in the original configuration are denoted by capital letters) and the deformed configuration of the body is denoted by b (all quantities in the deformed configuration are denoted by lower case letters). Consider an infinitesimal segment on the boundary of B. Let P be the point where the infinitesimal boundary segment is directed from, $\mathbf{X}$ be the position vector of P and $d\mathbf{X}$ be the vector representing the infinitesimal boundary segment. When the body deforms to the deformed configuration b, particle P moves to p and its position changes to $\mathbf{x}$. The boundary segment $d\mathbf{X}$ in the initial configuration deforms to $d\mathbf{x}$ in the deformed configuration. Note that the boundary segment changes not only in length but also in direction when it deforms. The displacement from P to p is denoted by vector $\mathbf{u}$. The physical quantities in the deformed configuration can be expressed by the corresponding physical quantities in the initial configuration (Lagrangian description) as described in Section III

$$\mathbf{x} = \mathbf{X} + \mathbf{u} \tag{36}$$
$$d\mathbf{x} = \mathbf{F}d\mathbf{X} \tag{37}$$

where $\mathbf{F}$ is the deformation gradient tensor given by (4). The components of the position and displacement vectors are given by

$$\mathbf{x} = \begin{Bmatrix} x \\ y \end{Bmatrix} \mathbf{X} = \begin{Bmatrix} X \\ Y \end{Bmatrix} \mathbf{u} = \begin{Bmatrix} u \\ v \end{Bmatrix} \text{ for } 2-D. \tag{38}$$

In the initial configuration, the infinitesimal boundary segment $d\mathbf{X}$ can be represented by the product of its length $d\Gamma$ and its unit direction vector $\mathbf{T}$. Similarly, the boundary segment $d\mathbf{x}$ in the deformed configuration can be represented by the product of its length $d\gamma$ and its unit direction vector $\mathbf{t}$

$$d\mathbf{x} = d\gamma \mathbf{t} \tag{39}$$
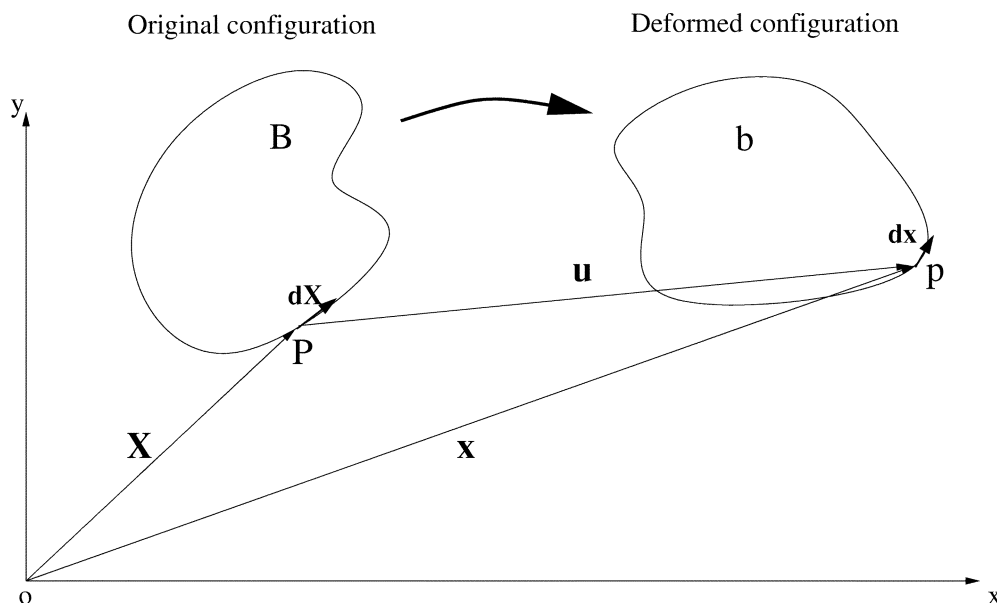$$d\mathbf{X} = d\Gamma \mathbf{T}. \tag{40}$$

Fig. 3. Various configurations of a deformable body.

By using the above relations, the geometry of a deformed structure can be expressed in terms of the geometry in the initial configuration and its deformation information. In the Lagrangian approach, we map the boundary integral equations in the deformed configuration, (34)–(35), to the initial configuration by representing each component in (34)–(35) by its counterpart in the initial configuration.

The electric potential ϕ on the conductors and the dielectric constant ϵ of the medium are constants in the deformed and the initial configurations. Using (36), the Green's function in two dimensions, $G(p, q)$, can be rewritten as

$$
\begin{aligned}
G(p,q) =& G\big(p(P), q(Q)\big) \\
=& -\frac{1}{2\pi\epsilon} ln|\mathbf{X}_P - \mathbf{X}_Q + \mathbf{u}_P - \mathbf{u}_Q|
\end{aligned}
\tag{41}
$$

where P and Q are the source and field points in the initial configuration corresponding to the source and field points p and q in the deformed configuration, $\mathbf{u}_P$ and $\mathbf{u}_Q$ are the displacements of points P and Q, respectively. For coupled electromechanical analysis, these displacements are computed by a mechanical analysis. Using (37), (39), and (40), the length of an infinitesimal line element, $d\gamma$, in the deformed configuration is expressed in terms of the length of the corresponding line element, $d\Gamma$, in the initial configuration by

$$
d\gamma\mathbf{t} = \mathbf{F}(d\Gamma\mathbf{T}).
\tag{42}
$$

Thus, we have

$$
\begin{aligned}
(d\gamma)^2 =& (d\gamma\mathbf{t}) \cdot (d\gamma\mathbf{t}) \\
=& [\mathbf{F}(d\Gamma\mathbf{T})] \cdot [\mathbf{F}(d\Gamma\mathbf{T})] \\
=& (d\Gamma)^2(\mathbf{T} \cdot \mathbf{F}^T\mathbf{F}\mathbf{T}).
\end{aligned}
\tag{43}
$$

The length of an infinitesimal line element in the deformed configuration can be written as

$$
d\gamma = d\Gamma(\mathbf{T} \cdot \mathbf{F}^T\mathbf{F}\mathbf{T})^{1/2}
\tag{44}
$$

or,

$$
d\gamma = d\Gamma(\mathbf{T} \cdot \mathbf{C}\mathbf{T})^{1/2}
\tag{45}
$$

where $\mathbf{C} = \mathbf{F}^T\mathbf{F}$ is the Green deformation tensor as introduced in (5). At a specified point q

$$
d\gamma_q = d\Gamma_Q\big(\mathbf{T}(Q) \cdot \mathbf{C}(Q)\mathbf{T}(Q)\big)^{1/2}.
\tag{46}
$$

Typically, the unknown quantity, such as the surface charge density, is approximated by using interpolation functions. In the deformed configuration, the surface charge density can be expressed as

$$
\sigma(\mathbf{x}) = \sum_i N_i(\mathbf{x})\hat{\sigma}_i
\tag{47}
$$

where $\sigma(\mathbf{x})$ is the surface charge density at $\mathbf{x}$, $\hat{\sigma}_i$ is the nodal parameter (constant) of the surface charge density at point i, and $N_i(\mathbf{x})$ is the interpolation function of point i evaluated at $\mathbf{x}$. If the surface charge density needs to be computed in the initial configuration, then (47) needs to be mapped to the initial configuration, i.e.,

$$
\sigma\big(\mathbf{x}(\mathbf{X})\big) = \sum_i N_i(\mathbf{X})\hat{\sigma}_i
\tag{48}
$$

where $\sigma\big(\mathbf{x}(\mathbf{X})\big)$ is the surface charge density in the initial configuration, $N_i(\mathbf{X})$ is the interpolation function of point i evaluated at $\mathbf{X}$ in the initial configuration.

The Lagrangian form of the boundary integral equations given in (34)–(35) is given by

$$
\begin{aligned}
\phi(P) =& \int_{d\Omega} G\big(p(P), q(Q)\big)\sigma\big(q(Q)\big) \\
& [\mathbf{T}(Q) \cdot \mathbf{C}(Q)\mathbf{T}(Q)]^{1/2} \, d\Gamma_Q + C
\end{aligned}
\tag{49}
$$

$$
\int_{d\Omega} \sigma\big(q(Q)\big) [\mathbf{T}(Q) \cdot \mathbf{C}(Q)\mathbf{T}(Q)]^{1/2} \, d\Gamma_Q = C_T
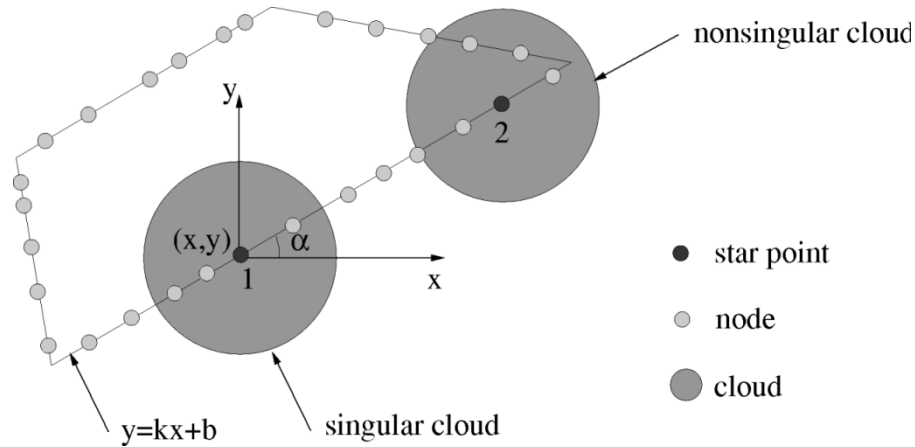\tag{50}
$$

Fig. 4.   Definition of singular and nonsingular cloud.

V. BCM FOR ELECTROSTATIC ANALYSIS

A BCM is employed to solve the Lagrangian boundary-integral form of the electrostatic equations [(49)–(50)]. In a BCM, the surface of the domain is discretized into scattered points. The points can be sprinkled randomly covering the boundary of the domain. Interpolation functions are constructed by centering a weighting function at each point or node. For the electromechanical problem, the potential ϕ is prescribed on the structures. The unknown surface charge density σ in the vicinity of the point t can be approximated by either a Hermite-type interpolation [14] or a varying basis least-squares approximation [15]. In this paper, we employ a varying basis least-squares approach to approximate the unknown surface charge density, i.e.,

$$\sigma^a(x,y) = \mathbf{p}_v^T(x,y)\mathbf{b}_t \qquad (51)$$

where $\mathbf{p}_v$ is the varying base interpolating polynomial, σ^a is an approximation to the unknown surface charge density σ, and $\mathbf{b}_t$ is the unknown coefficient vector for point t. To construct the varying basis interpolation functions, clouds are classified into two types: singular and nonsingular. When all of the points inside a cloud lie along a straight line, the cloud is defined as singular, otherwise, it is nonsingular. As shown in Fig. 4, the cloud of point 1 is singular and the cloud of point 2 is nonsingular, as the points do not lie along a straight line. In this paper, we use a linear polynomial basis. The base interpolating polynomial is given by

$$\mathbf{p}_v^T(x,y)$$
$$=\begin{cases} \begin{bmatrix} 1 & x & y \end{bmatrix} & m=3 \text{ (basis for nonsingular cloud)} \\ \begin{bmatrix} 1 & x \end{bmatrix} \text{ or } \begin{bmatrix} 1 & y \end{bmatrix} & m=2 \text{ (basis for singular cloud)} \end{cases}.$$
$$(52)$$

For a point t, the unknown coefficient vector $\mathbf{b}_t$ is computed by minimizing [28]

$$J_t = \sum_{i=1}^{NP} w_i(x_t, y_t)\left[\mathbf{p}_v^T(x_i,y_i)\mathbf{b}_t - \hat{\sigma}_i\right]^2 \qquad (53)$$

where NP is the number of nodes, $w_i(x_t, y_t)$ is the weighting function centered at (x_t, y_t) and evaluated at node i whose coordinates are (x_i, y_i) and $\hat{\sigma}_i$ is a nodal parameter. The weighting

function is typically a cubic spline or a Gaussian function as discussed in Section III. The stationary of J_t leads to

$$(\mathbf{P}_v^T\mathbf{W}\mathbf{P}_v)\mathbf{b}_t = \mathbf{P}_v^T\mathbf{W}\hat{\boldsymbol{\sigma}} \qquad (54)$$

which can be rewritten as

$$\mathbf{C}'_t\mathbf{b}_t = \mathbf{A}'_t\hat{\boldsymbol{\sigma}} \qquad (55)$$
$$\mathbf{b}_t = \mathbf{C}'^{-1}_t\mathbf{A}'_t\hat{\boldsymbol{\sigma}} \qquad (56)$$

where $\mathbf{C}'_t$ is an $m \times m$ matrix and $\mathbf{A}'_t$ is an $m \times NP$ matrix, whose definitions are given by

$$\mathbf{C}'_t = \mathbf{P}_v^T\mathbf{W}\mathbf{P}_v \qquad (57)$$
$$\mathbf{A}'_t = \mathbf{P}_v^T\mathbf{W} \qquad (58)$$

where

$$\mathbf{P}_v = \begin{bmatrix} \mathbf{p}_v^T(x_1,y_1) \\ \mathbf{p}_v^T(x_2,y_2) \\ \vdots \\ \mathbf{p}_v^T(x_{NP},y_{NP}) \end{bmatrix} \quad \hat{\boldsymbol{\sigma}} = \begin{bmatrix} \hat{\sigma}_1 \\ \hat{\sigma}_2 \\ \vdots \\ \hat{\sigma}_{NP} \end{bmatrix}$$

$$\mathbf{W} = \begin{bmatrix} w_1(x_t,y_t) & 0 & 0 & 0 \\ 0 & w_2(x_t,y_t) & 0 & 0 \\ 0 & 0 & \ddots & 0 \\ 0 & 0 & 0 & w_{NP}(x_t,y_t) \end{bmatrix}.$$
$$(59)$$

As shown in [14], when a cloud is singular, the moment matrix $\mathbf{C}'_t$ becomes singular if the full polynomial basis $[1\ x\ y]$ is used. In such cases, the appropriate base interpolating polynomial can be determined from the information of points contained in the cloud. For example, if all of the points in the singular cloud are defined by a line $y = $ constant, then $\mathbf{p}_v^T = [1\ x]$ can be used. If the singular cloud is defined by a line $x = $ constant, then $\mathbf{p}_v^T = [1\ y]$ can be used. In the general case of a cloud defined by $y = ax + b$, either $\mathbf{p}_v^T = [1\ x]$ or $\mathbf{p}_v^T = [1\ y]$ can be used. Substituting the definition of $\mathbf{b}_t$ from (56) into (51), the approximation for the unknown can be rewritten as

$$\sigma^a(x,y) = \mathbf{p}_v^T(x,y)\mathbf{b}_t = \mathbf{p}_v^T(x,y)\mathbf{C}'^{-1}_t\mathbf{A}'_t\hat{\boldsymbol{\sigma}}. \qquad (60)$$

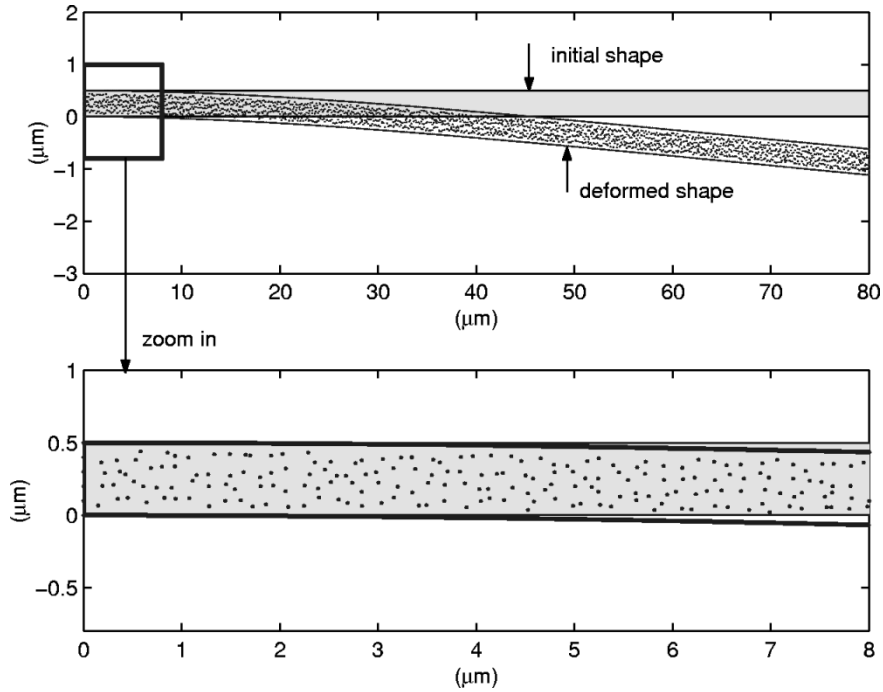Fig. 5. Deflection of a cantilever beam (not to scale) obtained with a scattered point distribution.

In short form

$$\sigma^a(x,y) = \overline{\mathbf{N}}(x,y)\hat{\boldsymbol{\sigma}} \tag{61}$$

where $\overline{\mathbf{N}}(x,y)$ is $1 \times NP$ interpolation vector given by

$$\overline{\mathbf{N}}(x,y) = \mathbf{p}_v^T(x,y)\mathbf{C'}_t^{-1}\mathbf{A'}_t. \tag{62}$$

$\overline{\mathbf{N}}(x,y)$ is again multivalued and the interpolation function can be limited to a single value by computing the interpolations at the point where the weighting function is centered (see [14] for details). Equation (61) can be rewritten in a matrix form as,

$$\boldsymbol{\sigma}^a = \overline{\mathbf{N}}\hat{\boldsymbol{\sigma}} \tag{63}$$

where $\overline{\mathbf{N}}$ is an $NP \times NP$ interpolation matrix. At any point (x,y), the unknowns are evaluated by

$$\sigma^a(x,y) = \sum_{I=1}^{NP} \overline{N}_I(x,y)\hat{\sigma}_I \tag{64}$$

where

$$\overline{N}_I(x,y) = \mathbf{p}_v^T(x,y)\mathbf{C'}_t^{-1}\mathbf{p}_v(x_I,y_I)w_I(x_t,y_t). \tag{65}$$

The discretized form of (49)–(50) is given by

$$\phi(P) = \sum_{k=1}^{NC} \int_{d\Omega} G(P,Q_k)\sigma(Q_k)$$
$$\cdot [\mathbf{T}(Q_k)\cdot\mathbf{C}(Q_k)\mathbf{T}(Q_k)]^{1/2}\, d\Gamma_Q + C \tag{66}$$

$$\sum_{k=1}^{NC} \int_{d\Omega} \sigma(Q_k)[\mathbf{T}(Q_k)\cdot\mathbf{C}(Q_k)\mathbf{T}(Q_k)]^{1/2}\, d\Gamma_Q = C_T. \tag{67}$$

Substituting (64) into (66)–(67) for each source node, the final matrix form is obtained as

$$\mathbf{Ax} = \mathbf{b}. \tag{68}$$

See equation (69)–(70) at the bottom of the page. The integrals in (69) are weakly singular and near singular when the source point P and the field point Q coincide or very close to each other, respectively. Regular Gauss quadrature becomes inaccurate in these cases. Special treatment is employed to compute

$$\begin{cases} A(i,j) = \sum_{k=1}^{NC} \int_{dS_k} G(P_i,Q_k)\overline{N}_j(Q_k)[\mathbf{T}(Q_k)\cdot\mathbf{C}(Q_k)\mathbf{T}(Q_k)]^{1/2}\, d\Gamma_Q & i,j = 1,\dots,NP \\ A(NP+1,j) = \sum_{k=1}^{NC} \int_{dS_k} \overline{N}_j(Q_k)[\mathbf{T}(Q_k)\cdot\mathbf{C}(Q_k)\mathbf{T}(Q_k)]^{1/2}\, d\Gamma_Q & j = 1,\dots,NP \\ A(i,NP+1) = 1 & i = 1,\dots,NP \\ A(NP+1,NP+1) = 0 & \end{cases} \tag{69}$$

$$\mathbf{x} = \begin{Bmatrix} \hat{\sigma}_1 \\ \hat{\sigma}_2 \\ \vdots \\ \hat{\sigma}_{NP} \\ C \end{Bmatrix} \quad \mathbf{b} = \begin{Bmatrix} \phi_1 \\ \phi_2 \\ \vdots \\ \phi_{NP} \\ C_T \end{Bmatrix}. \tag{70}$$
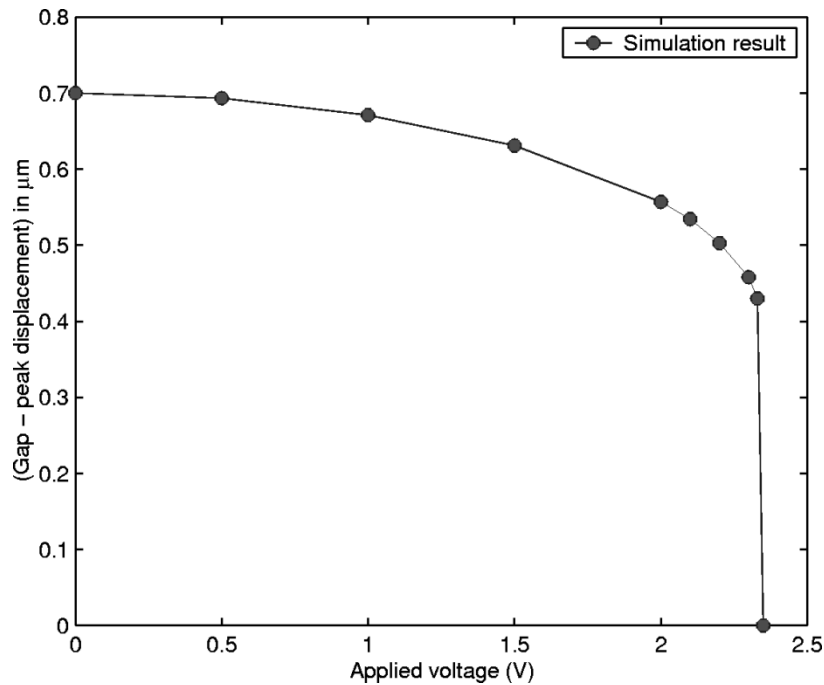
Fig. 6. (Gap–peak displacement) versus applied voltage for the cantilever beam. The pull-in voltage is 2.35 V.
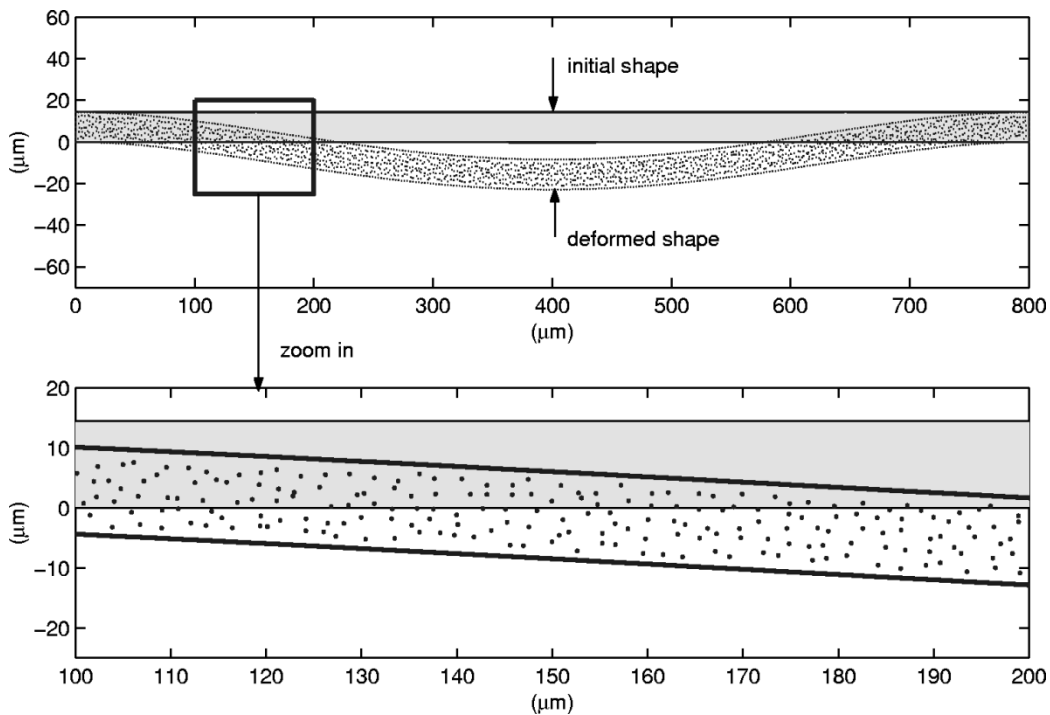

Fig. 7. Deflection of a fixed-fixed beam (not to scale) obtained with a scattered point distribution.

the various integrals. Given a source point P, cells are classified into three categories: 1) for cells which are far away from the source point, a regular Gauss quadrature is used to compute the integral; 2) for cells which are nearby to the source point, the weights of the nodes are computed more accurately by using the Nystrom [29] and the singular value decomposition (SVD) [30] techniques; and 3) for a cell which includes the source point, the integral is computed analytically. Extensive details on computing these integrals can be found in [14].

A. Remarks

1) When the same number of cells/elements are employed, the computational cost for BCM to compute the system matrices is higher compared to the standard BEM. However, it is shown in [22] that fewer cells are needed in BCM to achieve the same accuracy of BEM. The overall computational cost is actually less for BCM to obtain a similar solution of BEM.
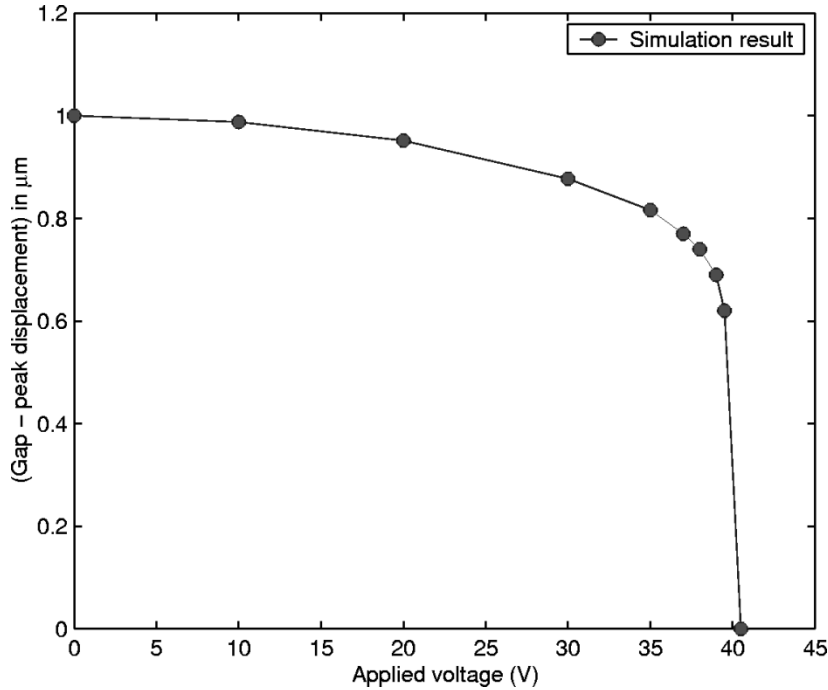
Fig. 8. (Gap–peak displacement) versus applied voltage for the fixed-fixed beam. The pull-in voltage is 40.5 V.
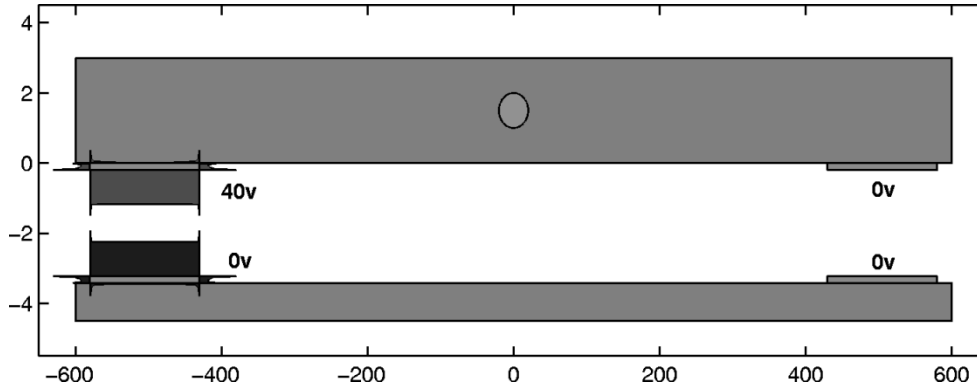

Fig. 9. Electrostatic micromirror structure (not to scale).

2) The additional computational cost for computing the matrices for Lagrangian electrostatics, i.e., ($[\mathbf{T}(Q_k) \cdot \mathbf{C}(Q_k)\mathbf{T}(Q_k)]^{1/2}$ in (69), is negligible (typically 5% more, see [16] for details).

The final dense linear system of equations [(68)] generated by the BCM are solved by a GMRES iterative solver combined with an SVD-based rapid matrix-vector multiplication technique [31]. The accelerated technique takes advantage of the fact that the integral equation kernel (2-D Green's function in our case) is locally smooth and, therefore, can be dramatically compressed by using an SVD technique. The acceleration technique greatly speeds up the solution phase of the linear system by accelerating the computation of the dense matrix-vector product and reducing the storage required by the BCM (see [31] for details). With the fast solver, the solution time for the electrostatic analysis scales as $O(N(\log(N)^2)$.

After the surface charge density for a node is computed, the electrostatic pressure can be computed by

$$P_e = \frac{\sigma^2}{2\epsilon}. \tag{71}$$

The electrostatic pressure in (71) is applied as the boundary condition for the mechanical analysis by using (8).

VI. NUMERICAL RESULTS

Five examples of electrostatic MEMS are considered in this section: a cantilever beam, a fixed-fixed beam, a torsional mirror, a lateral microactuator, and a comb drive device. The devices are simulated with scattered point distributions by using the methods described in the previous sections. The simulation results are compared with either experimental or previously reported data.

The first example is a cantilever beam over a ground plane. The cantilever beam is 80-μm-long, 10-μm-wide, 0.5-μ-thick, and is positioned 0.7-μm above the ground plane. The silicon beam has a Young's modulus of 169 GPa and a Poisson's ratio of 0.3. The beam is represented by 3606 scattered points (this is a much finer discretization—typically less than 1000 points are enough to get good accuracy) and the ground plane is discretized into 300 points. The point distribution is shown in Fig. 5. Fig. 6
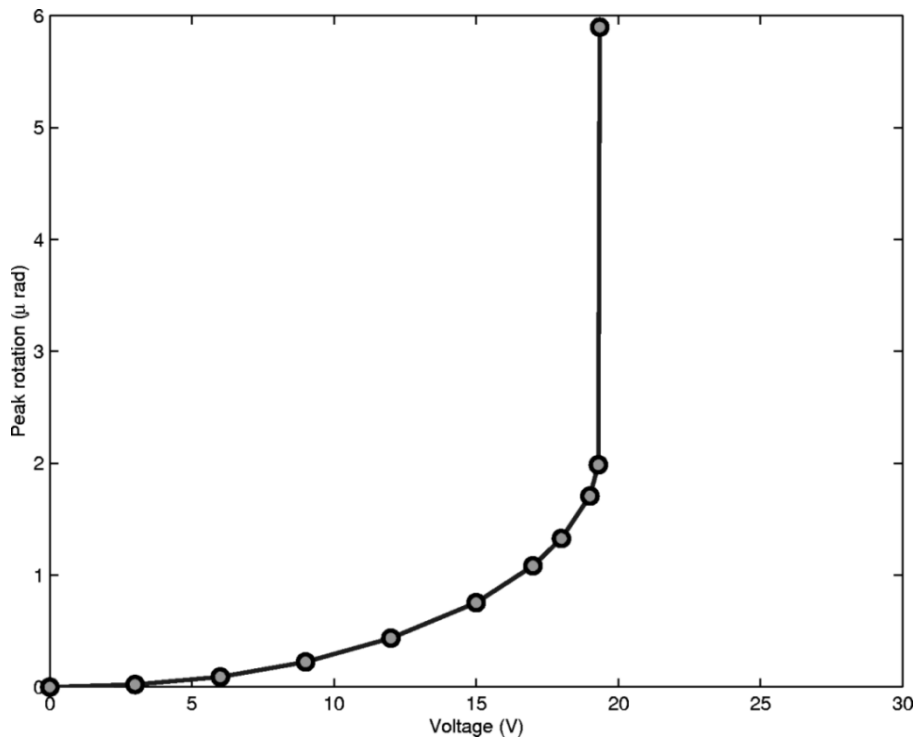
Fig. 10.   Peak rotation as a function of the applied voltage for the micromirror structure.
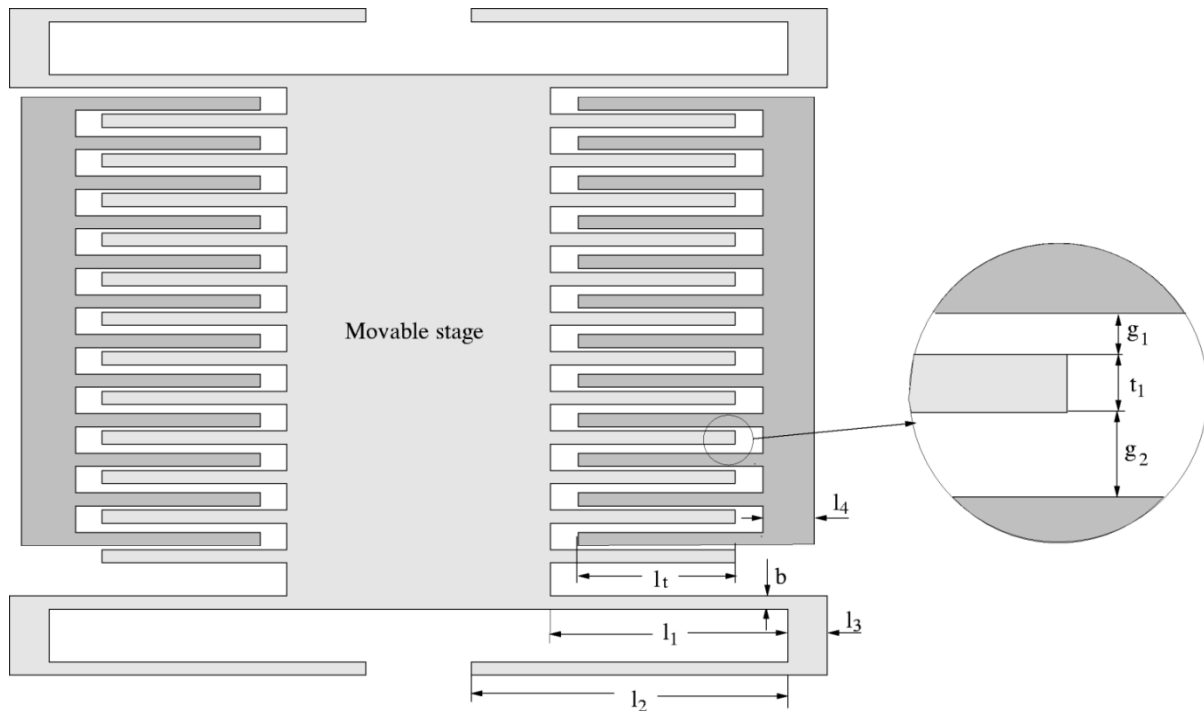

Fig. 11.   Lateral comb microactuator.

shows the peak deflection of the beam as a function of the applied voltage. The pull-in voltage for the cantilever beam is computed to be 2.35 V which compares well with a pull-in voltage of 2.39 V [10] for the same beam structure obtained by using an FEM/BEM approach.

The second example is a fixed-fixed beam over a ground plane. The geometry of the fixed-fixed beam is 800-μm-long, 50-μm-wide, and 14.4-μm-thick. The gap between the beam and the ground plane is 1 μm. The Young's modulus is 169 GPa and the Poisson's ratio is 0.3. The beam is represented by 2317 scattered points and the ground plane is discretized into 600 points. The point distributions are shown in Fig. 7. Fig. 8 shows the peak deflection of the beam as a function of the applied voltage. The computed pull-in voltage for the fixed-fixed beam
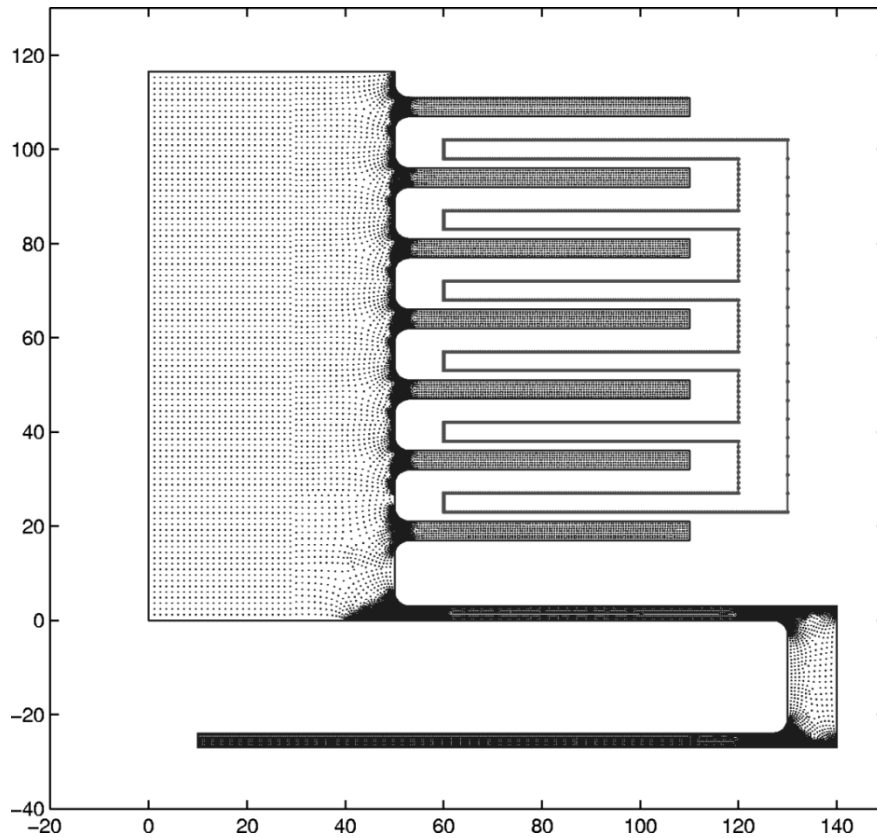
Fig. 12.   Lower right quadrant of the lateral comb microactuator with scattered point distribution.
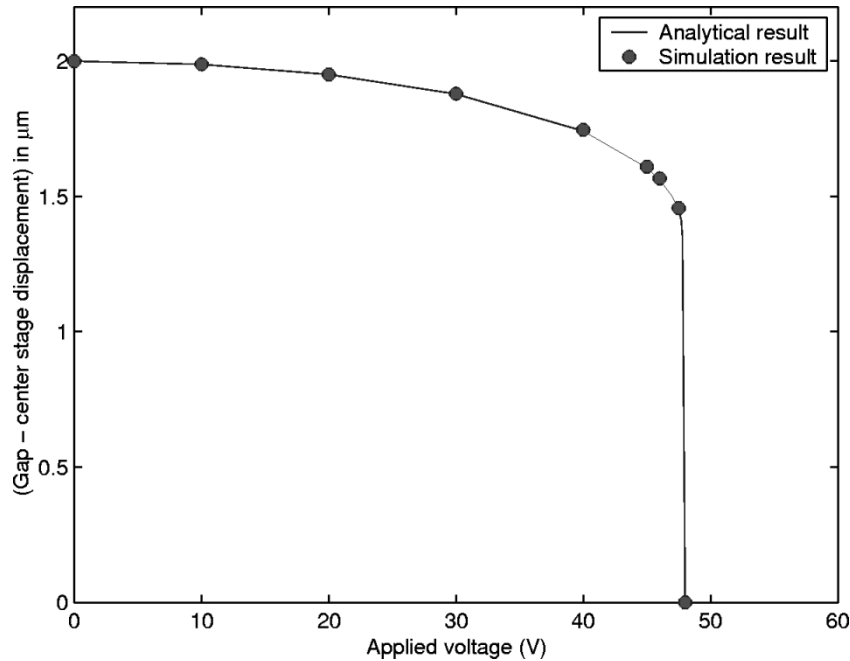

Fig. 13.   (Gap–center stage displacement) as a function of the applied voltage. The gap in this case is $g_1 = 2 \ \mu m$.

is 40.5 V which compares well with the pull-in voltage of 40 V [32] for the same beam structure obtained by the FEM/BEM technique.

The third example is the static analysis of a micromirror structure proposed in [33]. The configuration of the micromirror structure is shown in Fig. 9. The mirror plate is 1200-μm-long, 1300-μm-wide, and 3-μm-thick. Four 150-μm-long electrodes are attached to the mirror plate and the ground plane. The distance from the center of the electrodes on the mirror to the center of the mirror is 505 μm. The gap between each electrode pair is 3042 μm. Fig. 9 shows the surface charge density on the electrodes when a potential of 40 V is applied. The electrostatic
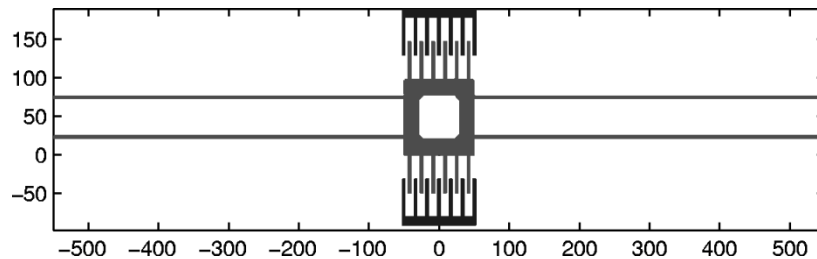
Fig. 14.   Electrostatic comb drive.

torque, with respect to the axis of the mirror plate, is computed by integrating the electrostatic pressure over the electrode surface. The rotation of the mirror is computed by

$$\alpha = \frac{M(\alpha)}{K_\alpha} \tag{72}$$

where $M(\alpha)$ is the electrostatic torque for a rotate angle of α and K_α is the spring torque constant. For the mirror structure $K_\alpha = 14.309 \ N\mu$m [33]. The peak rotation of the mirror structure as a function of the applied voltage is shown in Fig. 10. The computed pull-in voltage for the mirror structure is 19.3 V. The experimental data for this structure is reported in [33] and the reported pull-in voltage is 19.5 V which compares well with the computed pull-in value.

In the fourth example, static behavior of a lateral comb microactuator for hard disk head [34] is analyzed. The comb microactuator is shown in Fig. 11. The system consists of a movable stage, 24 pairs of interdigitated teeth and 4 spring beams. The center stage is supported by four folded spring beams. Electrostatic forces are generated when a voltage is applied between the fixed and movable structures. The center movable stage is 100-μm-long, 200-μm-wide, and 3.7-μm-thick. The other parameters are (see Fig. 11): $l_1 = 80 \ \mu$m, $l_2 = 120 \ \mu$m, $l_3 = 10 \ \mu$m, $l_4 = 10 \ \mu$m, $l_t = 50 \ \mu$m, $b = 3 \ \mu$m, $t_1 = 4 \ \mu$m, $g_1 = 2 \ \mu$m, and $g_2 = 5 \ \mu$m. The Young's modulus of the comb structure is 200 GPa and the Poisson's ratio is 0.31. Due to symmetry, it is sufficient to consider just the lower right quadrant of the device for coupled electromechanical simulation. The scattered point distribution for the device is shown in Fig. 12. Fig. 13 shows the moving distance of the center stage as a function of the applied voltage. The computed pull-in voltage of the microactuator is 48.0 V. For small displacements, the displacement of the movable stage can be obtained from analytical analysis [34]

$$\frac{nhl_t\epsilon_0}{2}\left\{\frac{1}{(g_1 - x)^2} - \frac{1}{(g_2 + x)^2}\right\}V^2 = 4Eh\frac{b^3}{l_1^3 + l_2^3}x \tag{73}$$

where n is the number of the teeth pair, h is the thickness of the structure, ϵ_0 is the permittivity of the free space, x is the lateral displacement of the moving stage, and V is the applied voltage. The curve shown in Fig. 13 is the analytical solution obtained form (73). The analytical pull-in voltage is 47.8 V. Fig. 13 shows that the simulation results agree quite well with the analytical solution. The experimental result given in [34] shows a lateral displacement of 0.55 μm at an applied voltage of 50 V. The experimental result is fairly close to the simulation and analytical results.

The final example is an electrostatic comb drive discussed in [35]. As shown in Fig. 14, a center mass with 12 teeth is
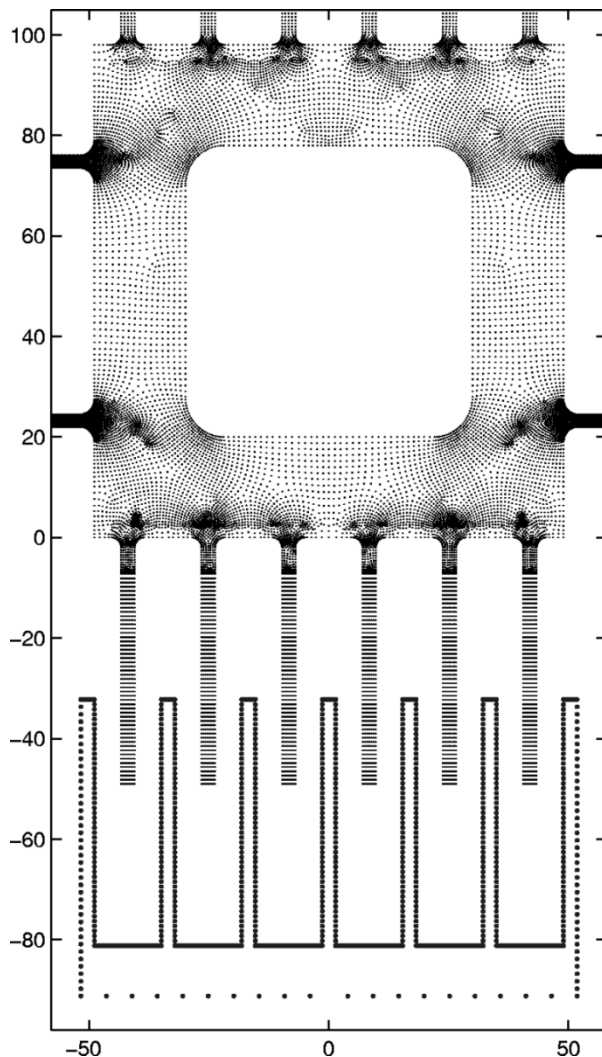

Fig. 15.   Closer look at the scattered point distribution for the center mass and some of the teeth attached to the center mass.

supported by fixed-fixed beams. A voltage is applied between the movable comb and the fixed teeth. The support beams are 1000-μm-long, 2.5-μm-wide, and 4.5-μm-thick. The center mass is 98 μm^2. Each comb tooth is 49-μm-long, 2.8-μm-wide, and 4.5-μm-thick. The gap between the movable teeth and the fixed teeth is 5.6-μm and the initial overlap at 0 V is 16.8-μm. The Young's modulus of the comb structure is 169 GPa and the Poisson's ratio is 0.3. The scattered point distribution for the device is shown in Fig. 15. Fig. 16 presents the computed displacement as a function of the applied voltage. Both linear [36] and nonlinear elastostatic theories are employed in this
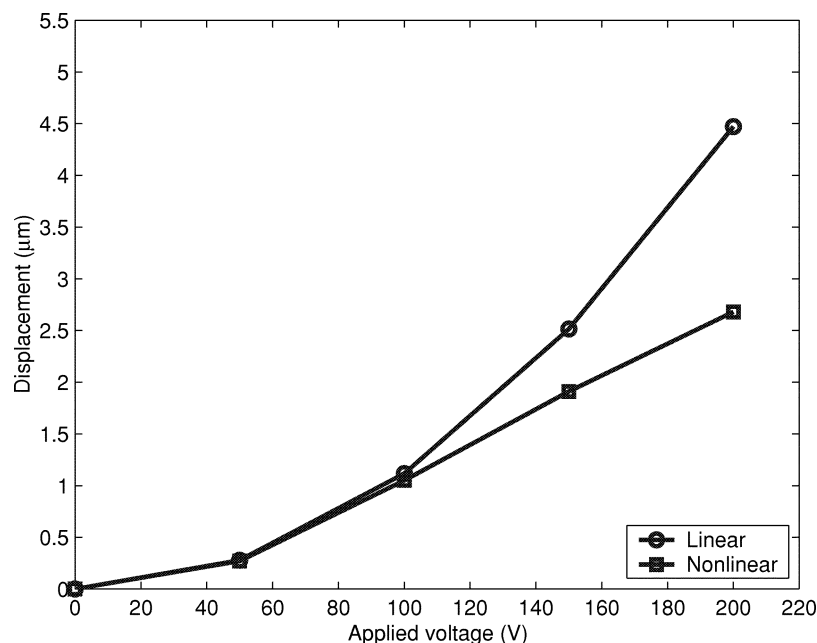
Fig. 16.   Simulation results with linear and nonlinear elastostatic theories for the peak displacement of the center mass.

example. As shown in Fig. 16, the comb structure starts to operate in a mechanically nonlinear regime for an applied voltage of 100 V or higher. The stiffness of the supporting beams increases quickly as the displacement of the center mass increases. Thus, for MEMS actuators where a large stroke is desired, the fixed-fixed type support is not advantageous due to the high stiffness of the support. For this reason, folded supporting beams are widely used in comb drive applications. The fixed-fixed support, however, provides a higher stability and a higher resistance to the external forces. Therefore, for applications such as force sensors the fixed-fixed support could still be an appropriate choice.

VII. CONCLUSION

We have presented a new combined FCM/BCM for efficient scattered point and meshless analysis of microelectromechanical devices. The hybrid FCM/BCM technique overcomes several inherent difficulties associated with the conventional FEM/BEM approach. The FCM/BCM approach requires only a scattered set of points and no connectivity information or a mesh is necessary. Even though the electrostatic analysis is coupled to the mechanical analysis through the same set of boundary nodes, the point distribution for electrostatic analysis can be refined without affecting the interior mechanical analysis. The Lagrangian electrostatics formulation combined with the well-known Lagrangian mechanical formulation allows coupled electromechanical analysis with only the initial configuration, there by eliminating the need for geometry updates and recalculation of interpolation functions. The hybrid FCM/BCM along with Lagrangian electrostatic and mechanical analysis radically simplifies self-consistent analysis of electrostatic MEMS.

REFERENCES

[1] S. Senturia, *Microsystem Design*.   Norwell, MA: Kluwer, 2001.
[2] ——, "CAD challenges for microsensors, microactuators, and microsystems," *Proc. IEEE*, vol. 86, pp. 1611–1626, Aug. 1998.
[3] T. Mukherjee, G. K. Fedder, D. Ramaswany, and J. K. White, "Emerging simulation approaches for micromachined devices," *IEEE Trans. Computer-Aided Design*, vol. 19, pp. 1572–1589, Dec. 2000.
[4] S. D. Senturia, R. M. Harris, B. P. Johnson, S. Kim, K. Nabors, M. A. Shulman, and J. K. White, "A computer-aided design system for microelectromechanical systems (MEMCAD)," *J. Microelectromechan. Syst.*, vol. 1, no. 1, pp. 3–13, 1992.
[5] T. Mukherjee and G. K. Fedder, "Structured design of microelectromechanical systems," in *Proc. 34th Design Automation Conf.*, Anaheim, CA, 1997, pp. 680–685.
[6] G. K. Fedder, "Structured design for integrated MEMS," in *Proc. IEEE MEMS*, 1999, pp. 1–8.
[7] G. K. Fedder and Q. Jing, "A hierarchical circuit-level design methodology for microelectromechanical systems," *IEEE Trans. Circuits Syst. II*, vol. 46, pp. 1309–1315, Oct. 1999.
[8] J. Clark, N. Zhou, S. Brown, and K. S. J. Pister, "Nodal analysis for MEMS simulation and design," in *Proc. Int. Conf. Modeling Simulation Microsyst.*, CA, 1998, pp. 308–313.
[9] G. T. A. Kovas, *Micromachined Transducers Sourcebook*.   New York: McGraw-Hill, 1998.
[10] N. Aluru and J. White, "An efficient numerical technique for electromechanical simulation of complicated microelectromechanical structures," *Sensors Actuators A*, vol. 58, pp. 1–11, 1997.
[11] J. R. Gilbert, R. Legtenberg, and S. D. Senturia, "3D coupled electromechanics for MEMS: Applications of CoSolve-EM," in *Proc. MEMS*, 1995, pp. 122–127.
[12] N. R. Aluru and G. Li, "Finite cloud method: A true meshless technique based on a fixed reproducing kernel approximation," *Int. J. Numer. Methods Eng.*, vol. 50, no. 10, pp. 2373–2410, 2001.
[13] X. Jin, G. Li, and N. R. Aluru, "On the equivalence between least-squares and kernel approximation in meshless methods," *Comput. Modeling Eng. Sci.*, vol. 2, no. 4, pp. 447–462, 2001.
[14] G. Li and N. R. Aluru, "Boundary cloud method: A combined scattered point/boundary integral approach for boundary-only analysis," *Comput. Methods Appl. Mechanics Eng.*, vol. 191, no. 21–22, pp. 2337–2370, 2002.
[15] ——, "A boundary cloud method with a cloud-by-cloud polynomial basis," *Eng. Anal. Boundary Elements*, vol. 27, no. 1, pp. 57–71, 2003.
[16] ——, "A lagrangian approach for electrostatic analysis of deformable conductors," *J. Microelectromechan. Syst.*, vol. 11, no. 3, pp. 245–254, 2001.
[17] T. J. R. Hughes, *The Finite Element Method*.   Englewood Cliffs, NJ: Prentice-Hall, 1987.
[18] J. H. Kane, *Boundary Element Analysis in Engineering Continuum Mechanics*.   Englewood Cliffs, NJ: Prentice-Hall, 1994.

[19] N. R. Aluru, "A point collocation method based on reproducing kernel approximations," *Int. J. Numer. Methods Eng.*, vol. 47, pp. 1083–1121, 2000.

[20] X. Wang, J. N. Newman, and J. White, "Robust algorithms for boundary-element integrals on curved surfaces," in *Proc. 3rd Int. Conf. Modeling Simulation Microsyst., Semiconduct., Sensors Actuators*, 2000, pp. 473–476.

[21] G. Li, G. H. Paulino, and N. R. Aluru, "Coupling of the meshfree finite cloud method with the boundary element method: A collocation approach," *Comput. Methods Appl. Mechanics Eng.*, vol. 192, no. 20–21, pp. 2355–2375, 2003.

[22] V. Shrivastava and N. R. Aluru, "A Fast Boundary Cloud Method for 3D Exterior Electrostatic Analysis," Int. J. Numer. Methods Eng., 2003, to be published.

[23] D. S. Chandrasekharaiah and L. Debnath, *Continuum Mechanics*. New York: Academic, 1994.

[24] T. Belytschko, Y. Krongauz, D. Organ, M. Fleming, and P. Krysl, "Meshless methods: An overview and recent developments," *Comput. Methods Appl. Mech. Eng.*, vol. 139, pp. 3–47, 1996.

[25] J. D. Jackson, *Classical Electrodynamics*, 3rd ed. New York: Wiley, 1999.

[26] F. Shi, P. Ramesh, and S. Mukherjee, "On the application of 2D potential theory to electrostatic simulation," *Commun. Numer. Methods Eng.*, vol. 11, pp. 691–701, 1995.

[27] Y. X. Mukherjee and S. Mukherjee, "The boundary node method for potential problems," *Int. J. Numer. Methods Eng.*, vol. 40, pp. 797–815, 1997.

[28] P. Lancaster and K. Salkauskas, "Surface generated by moving least squares methods," *Math. Computation*, vol. 37, pp. 141–158, 1981.

[29] S. Kapur and D. E. Long, "High-order Nyström schemes for efficient 3-d capacitance extraction," in *Proc. 38th Int. Conf. Computer-Aided Design*, San Jose, CA, 1998, pp. 178–185.

[30] G. H. Golub and C. F. Van Loan, *Matrix Computations*. Baltimore, MD: The Johns Hopkins University Press, 1989.

[31] V. Shrivastava and N. R. Aluru, "A fast boundary cloud method for exterior 2-D electrostatics," *Int. J. Numer. Methods Eng.*, vol. 56, no. 2, pp. 239–260, 2003.

[32] P. M. Osterberg and S. D. Senturia, "M-test: A test chip for MEMS material property measurement using electrostatically actuated test structures," *J. Microelectromechan. Syst.*, vol. 6, no. 2, pp. 107–118, 1997.

[33] O. Degani, E. Socher, A. Lipson, T. Leitner, D. J. Setter, S. Kaldor, and Y. Nemirovsky, "Pull-in study of an electrostatic torsion microactuator," *J. Microelectromechan. Syst.*, vol. 7, no. 4, pp. 107–118, 1998.

[34] T. Imamura, M. Katayama, Y. Ikegawa, T. Ohwe, R. Koishi, and T. Koshikawa, "MEMS-based integrated head/actuator/slider for hard disk drives," *IEEE/ASME Trans. Mechatronics*, vol. 3, no. 3, pp. 166–174, 1998.

[35] M. A. Rosa, S. Dimitrijev, and H. B. Harrison, "Improved operation of micromechanical comb-drive actuators through the use of a new angled comb finger design," *J. Intell. Material Syst. Structures*, vol. 9, pp. 283–290, 1998.

[36] G. Li and N. R. Aluru, "Linear, nonlinear and mixed-regime analysis of electrostatic MEMS," *Sensors Actuators A*, vol. 91, no. 3, pp. 278–291, 2001.

Gang Li (S'02) received the B.S. and M. Eng. degrees in mechanical engineering from Tongji University, Shanghai, P.R. China, in 1993 and 1996, respectively, and the M.Asc. degree in mechanical engineering from Dalhousie University, Halifax, NS, Canada, in 1999. He is currently pursuing the Ph.D. degree in mechanical engineering at the University of Illinois, Urbana–Champaign.

His research interests include computational analysis and design of MEMS and numerical methods in engineering.

N. R. Aluru (M'00) received the B.E. degree (honors and distinction) from the Birla Institute of Technology and Science, Pilani, India, in 1989, the M.S. degree from Rensselaer Polytechnic Institute, Troy, NY, in 1991, and the Ph.D. degree from Stanford University, Stanford, CA, in 1995.

He was a Post-Doctoral Associate at the Massachusetts Institute of Technology, Cambridge, MA, from 1995 to 1997. In 1998, he joined the Department of General Engineering, University of Illinois, Urbana–Champaign (UIUC), where he is currently a Willett Faculty Scholar and an Associate Professor. He is affiliated with the Beckman Institute for Advanced Science and Technology, Department of Electrical and Computer Engineering, and the Mechanical and Industrial Engineering at UIUC. His current research interests are in the areas of computational methods, MEMS/NEMS, micro- and nano-fluidics, Bio-MEMS, and bionanotechnology.

Prof. Aluru received the 1999 National Science Foundation CAREER award, the 1999 NCSA faculty fellowship, a 2001 CMES Distinguished Young Author Award, and a 2002 Xerox Award.